Electronic structure effects in spatiotemporally resolved photoemission interferograms of copper surfaces

M. J. Ambrosio and U. Thumm

Phys. Rev. A **96**, 051403 — Published 20 November 2017

DOI: 10.1103/PhysRevA.96.051403

Electronic structure effects in spatiotemporally-resolved photoemission interferograms of copper surfaces

M. J. Ambrosio and U. Thumm
Department of Physics, Kansas State University, Manhattan, KS 66506, USA
(Dated: November 8, 2017)

Attosecond photoelectron spectroscopy allows the observation of electronic processes on attosecond timescales (1 as = 10^{-18} seconds), as has been demonstrated in proof-of-principle experiments that probe the electronic dynamics in isolated atoms with unprecedented accuracy. Its recent expansion to solid targets is starting to allow the distinction of ultrafast collective electronic processes in matter with added spatial resolution, probing the electronic band structure and dielectric response in nanoplasmonically enhanced light-induced processes of relevance for photocatalysis, optoelectronics, and light harvesting. Based on a quantum-mechanical model for photoelectron emission by an attosecond pulse train from the *d* band of a Cu(111) surface into a delayed assisting laser pulse, we calculate two-pathway two-photon interferograms as functions of the photoelectron energy and pulse delay. Our results scrutinize the dependence of observable photoelectron interferograms on the electronic structure of and electron transport in the substrate and agree well with experimental spectra and semiclassical Monte-Carlo simulations of Lucchini *et al.* [Phys. Rev. Lett. **115**, 137401 (2015)].

Based on the process of higher harmonics (HHs) generation in atomic gases [1, 2], continued progress in ultrafast laser technology enabled the superposition of HHs to attosecond pulse trains (APTs) [3] and isolated attosecond pulses (IAPs) [4, 5] that are perfectly synchronized with the driving infrared (IR) laser, allowing for time-resolved investigations of the electronic dynamics in gases and condensed matter systems. These time-domain investigations complement traditional energy-domain spectroscopies [6] and are implemented in two types of experimental setups, streaked photoelectron emission and reconstruction of attosecond beating by interference of two-photon transitions (RABBITT). In streaking experiments, photoelectrons are emitted by a spectrally broad extreme ultraviolet (XUV) IAP into the electric field of a delayed infrared pulse [7]. Recording photoelectron energy spectra as a function of the IAP - IR delay reveals temporal information through delay-dependent photoelectron energy shifts, reducing the measurement of ultrashort time-intervals (of the order of 10 as, 1 atomic unit of time = 1 a.u. = 24 as) to conveniently detectable photoelectron energies. Instead of IAPs, RABBITT experiments employ XUV APTs to emit electrons into a synchronized delayed IR pulse, imaging electric dynamics as photoelectron-yield oscillations due to two two-photon quantum-pathway interference [3] (Fig. 1). While RABBITT spectra have been analyzed to probe isolated atoms in the gas phase for some time [3, 8, 9], so far their recording and analysis for solid targets has been limited to just a few recent experimental [10–13] and theoretical [14, 15] investigations.

While encoding the same basic information on the static and dynamic substrate electronic structure as streaked spectra, RABBITT interferograms are more conveniently obtained in the laboratory, since APTs are easier to generate than IAPs and require lower IR intensities (typically 10^{11} W/cm^2) [10–13]), thus distorting the target less and facilitating their interpretation in terms of two two-photon (absorption of one XUV and absorption/emission of one IR photon, as opposed to pathways including more than one IR photon). In order to eliminate the unknown phases $\{\phi^{HH}_{2n+1}\}$ of the odd-order HH constituents of the ATP, recent experiments either (i) subtracted RABBITT interferograms obtained in the same experiment on metal surfaces and a reference gas target [10, 11] or (ii) compared relative phases ("RABBITT phases") in the delay-dependent yield oscillations from energetically separable initial states of the same solid target [12]. In addition to temporal information, RABBITT spectra from solid targets reveal details on the spatial distribution of the initial electronic probability density and the dispersion and scattering of APT-excited photoelectrons inside the solid prior to their emission [13, 15].

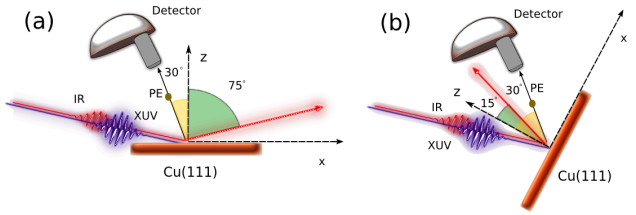

Figure 1: (Color online) (a) RABBITT experimental setup of Lucchini *et al.* [11]. Linearly *p* polarized XUV APTs and time-delayed IR pulses are incident at 75° on a Cu(111) surface, while photoelectrons emitted in the reflection plane are detected under -30° with respect to the surface normal. (b) Same as (a) for 15° pulse incidence and 30° electron detection.

Besides their complex electronic structure, solid targets require the inclusion of macroscopic effects in the reflection of the assisting IR pulse for the computation and analysis of RABBITT spectra [10–12, 14, 15]. This is of particular importance for the considered copper surfaces that reflect most of the incident IR intensity and entail distinct Fresnel reflection rates for the two incidence an-

gles realized by Lucchini *et al.* [11] (Fig. 1). In this Letter we present a quantum-mechanical model for the laser assisted XUV photoemission from metal surfaces and apply this model to the RABBITT experiment presented in Ref. [11]. Accordingly, we assume the XUV pulse train vector potential $\mathbf{A}_{XUV}(z,t)$ to be composed of odd HH orders n =15 to 23, each having a spectral width of 1 eV [10]. The XUV ATPs propagates unimpeded through the few monolayers below the copper surface, from where photoelectrons are detected [15]. Our numerical results will be shown to allow for (i) the scrutiny of contributions from interfering photoemission pathways involving more than one IR photon, and the investigation of the dependence of observable interferograms on the (ii) substrate's IR dielectric response, (iii) ground-state electronic structure, and (iv) photoelectron dispersion. Unless specified otherwise, we use atomic units throughout.

Integrating around the emission direction $\Omega_f = (\theta_f, \varphi_f = 0^\circ)$ in the reflection plane over a solid-angle interval $\Delta\Omega_f = (\Delta\theta_f, \Delta\varphi_f) = (10^\circ, 5^\circ)$ for a given delay τ between the IR-pulse and the ATP centers, and for a photoelectron final energy $\varepsilon_f = k_f^2/2$, incoherent summation over all occupied initial valence-band (VB) states below the Fermi level leads to the energy-differential photoemission yield

$$P(\varepsilon_f, \tau) = \sqrt{2\varepsilon_f} \int_{\Delta\Omega_f} d\Omega_f \sum_{|\mathbf{k}_i|<k_F} \left| T_{\mathbf{k}_f,\mathbf{k}_i}(\tau) \right|^2, \quad (1)$$

where k_F is the Fermi momentum. Representing the transition matrix element in the non-dipole velocity gauge,

$$T_{\mathbf{k}_f,\mathbf{k}_i}(\tau) \propto \quad (2)$$
$$\int_{-\infty}^{\infty} dt \left\langle \Psi^f_{\mathbf{k}_f}(\mathbf{r},t,\tau) \left| \mathbf{A}_{XUV}(z,t)\cdot\nabla \right| \Psi^i_{\mathbf{k}_i}(\mathbf{r},t) \right\rangle,$$

we do not impose restrictions on the size of the illuminated target volume and electron-emission direction [15–17].

We approximate the initial VB state as translationally invariant in the surface (x-y) plane, $\Psi^i_{\mathbf{k}_i}(\mathbf{r},t) = e^{\mathbf{k}_{i,\parallel}\cdot\mathbf{r}_\parallel}\phi_{n,k_{i,z}}(z)\, e^{-iE_b t}$, where $\mathbf{k}_{i,\parallel} = (k_{i,x}, k_{i,y})$ and $\mathbf{r}_{i,\parallel} = (x,y)$, and expand along the surface normal (z) direction in localized Hulthén Generalized Sturmian Functions (GSFs) [20, 21] centered at each atomic plane j,

$$\phi_{n,k_{i,z}}(z) = \sum_j e^{ik_{iz}z_j} \varphi_n(E_{TB}, \alpha_H, |z - z_j|). \quad (3)$$

The localized GSFs

$$\varphi_n(E_{TB}, \alpha_H, u) \propto e^{-\kappa u} \quad (4)$$
$$ {}_2F_1\left[-n, 2\alpha_H\kappa + n, 2\alpha_H\kappa, e^{-u/\alpha_H}\right],$$

model the active electron in the screened Coulomb field of its parent lattice plane, $\mathcal{V}(u) = \frac{\exp(-u/\alpha_H)}{1-\exp(-u/\alpha_H)}$, with an adjustable energy E_{TB}, corresponding to the rate of exponential decay of the electron's probability density with the distance $u = z - z_j$. They are written in terms of hypergeometric functions ${}_2F_1$ as solutions of the 1D Hulthén generalized-eigenvalue problem $\left[-\frac{1}{2}\frac{d^2}{du^2} + \beta_n\mathcal{V}(u) - E_{TB}\right]\varphi_n(E_{TB}, \alpha_H, u) = 0$ with $\kappa = \sqrt{-2E_{TB}}$ and for $u \geq 0$ [20]. We select GSFs with positive parity by defining $\varphi_n(E_{TB}, \alpha_H, u) \equiv \varphi_n(E_{TB}, \alpha_H, -u)$ for $z < z_j$. α_H determines the nodal structure of $\varphi_n(E_{TB}, \alpha_H, u)$ near its parent lattice plane. For our numerical applications discussed below, we select Cu(111) $3d$ orbitals with a single node (setting $n = 1$) and adjust $\alpha_H = 0.2a_s$ with the Cu(111) interlayer spacing $a_s = 3.94$ [22]. The generalized eigenvalue β_1 corresponds to an effective core charge and is determined by the adjustable parameters E_{TB} and α_H. A similar tight-binding approach [16] based on charge-scaled hydrogenic ground-state wave functions (HGWFs) was found suitable to model Pt(111) core levels (see [18, 19] with regard to the localization properties of the Cu d-band). We note, however, that the present expansion in terms of GSFs with two adjustable parameters allows a more versatile representation of the target electron structure than the use of HGWFs in Ref. [16].

We model the final state based on Volkov functions for the interaction of the free electron with homogeneous continuum-wave electric fields [16],

$$\Psi^f_{\mathbf{k}_f}(\mathbf{r},t,\tau) = \frac{f_{\varepsilon_f,\theta_f}(z)}{(2\pi)^{3/2}} e^{i\mathbf{k}_{f,\parallel}\cdot\mathbf{r}_\parallel} \quad (5)$$
$$\times\psi_{k_{f,z}}(z,t_d) e^{i\phi_{\mathbf{k}_f}(z,t_d)} e^{-i\varepsilon_f t},$$

with $t_d = t - \tau$ and $\mathbf{k}_{f,\parallel} = (k_{f,x}, k_{f,y})$, including three heuristic modifications: (i) Inside the substrate ($z < 0$) we introduce the energy-dependent mean free path $\lambda(\varepsilon_f)$ with the damping factor

$$f_{\varepsilon_f,\theta_f}(z<0) = e^{z/[2\lambda(\varepsilon_f)\cos(\theta_f)]}, \quad (6)$$

in order to account for the loss of emission probability from deeper layers, setting $f_{\varepsilon_f,\theta_f}(z>0) = 1$ and using the numerical values for $\lambda(\varepsilon_f)$ of Ref. [23]. (ii) With

$$\psi_{k_{f,z}}(z) = \begin{cases} e^{ik_{f,z}z}, & z \geq 0 \\ \psi^{well}_{k_{f,z}}(z), & z < 0 \end{cases} \quad (7)$$

we include the energy loss and partial reflection of the photoelectron at the surface ($z = 0$) in terms of the outgoing plane wave $e^{ik_{f,z}z}$ with asymptotic momentum component $k_{f,z}$ that matches with continuous derivative the superposition of a substrate-bound plane wave with momentum $k^{in}_{f,z} = \sqrt{(k_{f,z})^2 + 2U_0}$ and its reflection into the bulk at a potential step of height U_0 at the surface,

$$\psi^{well}_{k_{f,z}}(z) = \cos(k^{in}_{f,z}z) - i\frac{k_{f,z}}{k^{in}_{f,z}}\sin(k^{in}_{f,z}z). \quad (8)$$

Including the effect of $U_0 > 0$ on the final photoelectron state strongly affects photoelectron spectra, as will be

shown below. This inclusion of U_0 in $\psi_{k_{f,z}}$ extends the representation of the final state in Ref. [16] in terms of exponentially screened Volkov wave functions and is supported by recent experimental evidence for a distinct non-free-electron character of photoelectrons emitted from Ni(111) surfaces [12]. (iii) Generalizing the Volkov phase as

$$\phi_{\mathbf{k}_f}(z,t) = \int_t^\infty dt' \mathbf{k}_{f,\parallel} \cdot \mathbf{A}_{IR,\parallel}(z,t') + \int_t^\infty dt' A_{IR,z}(z,t') \begin{cases} k_{f,z}, & z > 0 \\ k_{f,z}^{in}, & z < 0 \end{cases}, \quad (9)$$

with $\mathbf{A}_{IR,\parallel} = (A_{IR,x}, A_{IR,y})$, we allow for *inhomogeneous* IR vector potentials $\mathbf{A}_{IR}(z,t) = \int_t^\infty \mathbf{E}_{IR}(z,t')\,dt'$. The spatial dependence of $\phi_{\mathbf{k}_f}(z,t)$ is due to both, Fresnel reflection of the incident IR pulse and the inclusion of $U_0 > 0$. In the limit of homogenous IR fields $\mathbf{A}_{IR}(t)$, Eq. (9) yields the phase of Volkov wavefunctions [16].

We determine the transmitted and reflected electric fields of the assisting IR pulse from Fresnel's equations [15, 24], employing a Lorentz-Drude-model complex-valued dielectric function $\varepsilon(\omega_{IR})$ [25]. Since Fresnel's equations are macroscopic in nature, implying a discontinuous change of the electric field at the interface, we introduce the gradual transition function

$$\mu(z) = e^{(z-z_{IR})/\delta_{IR}}, \; z < z_{IR}, \quad (10)$$

exponentially damping the total external IR field inside the substrate. We use the IR-pulse intensity, photon energy, and pulse width specified in Ref. [11] [5×10^{11} W/cm^2, 1.557 eV (786 nm wavelength), and 10 fs] and adjust the IR skin depth $\delta_{IR} = 2.25a_s$ and the decay-onset position $z_{IR} = 0.75a_s$ for best overall visual agreement with the experimental interferograms. Evaluating the transition matrix (2), we approximate the IR field screening by a stepwise decay, assuming $\mu(z) \approx \mu(z_j)$ across each atomic layer j. This allows us to perform the z and t integrations in (2) analytically.

In Fig. 2 we compare our calculated RABBITT interferograms with the experimental spectra of Ref. [11]. We adjusted the delay axis in our spectra for maximal overlap between the XUV APT and IR pulse to occur at τ =-1.8 fs and -0.84 fs, respectively, for 75° and 15° incidence. For 75° incidence we observe sideband (SB) peaks to have a larger temporal width than HH peaks [Figs. 2(a,b)] in obvious deviation from the expected [3] $\cos(2\omega_{IR}\tau)$ yield oscillation. We attribute this deviation to interference terms between quantum pathways collectively involving more than two IR-photons. We designate the transition matrix element of a photoemission pathway involving the absorption of a $(2n+1)\omega_{IR}$ XUV photon and the absorption (emission) of m IR photons as T^m_{2n+1} (T^{-m}_{2n+1}). The coherent superposition of all involved T^m_{2n+1} generates the observed photoelectron yield oscillations.

To lowest order, $\cos(2\omega_{IR}\tau)$ HH-yield oscillations originate in $T^0_{2n+1} \cdot T^{-2}_{2n+3}$ and $T^0_{2n+1} \cdot T^{+2}_{2n-1}$ interferences. The expected [3] $\cos(2\omega_{IR}\tau)$ SB oscillations stem from the interference $T^{+1}_{2n-1} \cdot T^{-1}_{2n+1}$. The narrowing of the HH and widening of SB peaks [relative to $\cos(2\omega_{IR}\tau)$, Figs. 3(a,b)] thus indicates contributions from pathway combinations adding up to four IR photons. These contributions are less noticeable at 15° incidence due to the smaller net IR electric-field component along the electron-emission direction $\mathbf{k}_f$. For 15° incidence, the generalized Volkov phase (9) in (2) thus oscillates with a smaller amplitude, reducing the number of relevant multipoles (and hence the number of photons) in the expansion $e^{i\phi_{\mathbf{k}_f}(z,t_d)} = 1 + i\phi_{\mathbf{k}_f}(z,t_d) - \phi^2_{\mathbf{k}_f}(z,t_d) + \ldots$ in (5).

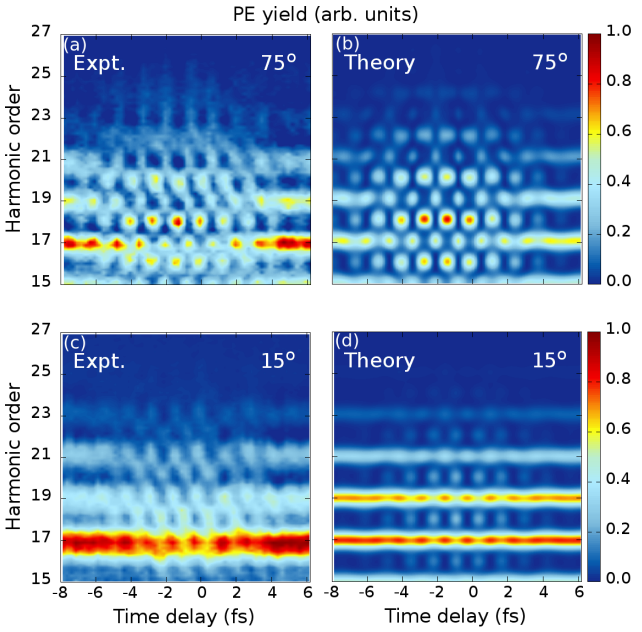

Figure 2: (Color online) RABBITT interferograms for (a,b) 75° and (c,d) 15° incidence, normalized separately. (a,c) Experiment [11]. (b,d) Theory.

The $4\omega_{IR}$ HH oscillations result from the three possible combinations of interfering multi photon processes depicted in Fig. 4(a), $T^{-2}_{2n+3} \cdot T^{+2}_{2n-1}$, and Figs. 4(b,c), $T^0_{2n+1} \cdot T^{\mp 4}_{2n+1\pm 4}$. We observed the peak heights in Fig. 3(b) of the $4\omega_{IR}$ peaks to change by roughly 25 %, when excluding the pathways involving four IR photons shown in Figs. 4(b,c), demonstrating that all two-path interferences in Fig. 4 contribute to the observed HH yield. Analogously, the lowest order pathway interferences that lead to $4\omega_{IR}$ oscillations in a given SB_{2n} are $T^{\mp 1}_{2n\pm 1} \cdot T^{\pm 3}_{2n\mp 3}$.

In order to assess to what extent RABBITT interferograms are sensitive to the Cu(111) electronic structure, we illustrate in Fig. 5 the variation of simulated spectra with changes of parameters in our model. We find that changing $\lambda(\varepsilon_f)$ with respect to the values tabulated in [23] by a factor of four significantly modifies RABBITT spectra, while a factor of two does not [Fig. 5(a)]. Figure 5(b) shows energy profiles for 75° incidence cal-

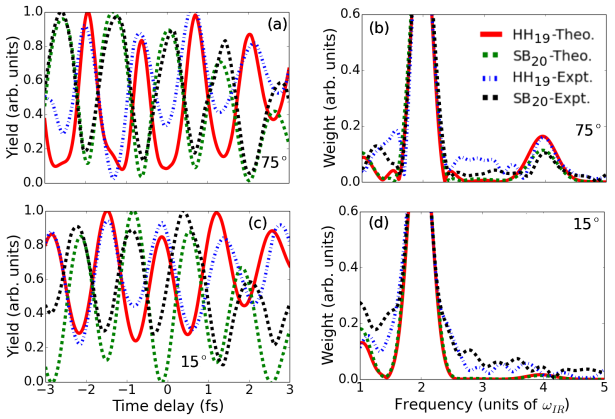

Figure 3: (Color online) (a) Measured [11] and calculated oscillations in the photoelectron yields integrated over 0.3 eV intervals around HH_{19} and SB_{20} energies for 75° incidence. (b) Fourier transform of (a) with frequencies in units of ω_{IR}. (c,d) Same as (a,b) for 15° incidence.

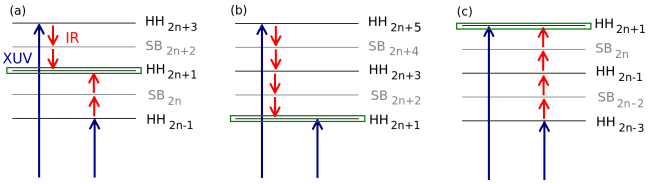

Figure 4: (Color online) Interfering photoemission pathways leading to $4\omega_{IR}$ oscillations in the HH yields in Fig. 3. (a) Two two-IR-photon transitions. (b,c) Zero-IR-photon and a four-IR-photon transitions.

culated for the maximum, minimum, and average bulk value the oscillating Chulkov potential [22]. The theoretical interferograms agree better with the two experiments when the effect of the potential step on $\Psi^f_{\mathbf{k}_f}$ is included. The agreement is best when U_0 is adjusted to the Chulkov-potential minimum, $U_0 = 17.035$ eV, the value adopted for the calculated spectra in Fig. 2. The influence of the IR-skin-depth on the energy profile around the value that yields the best comparison with both measured spectra, $\delta_{IR} = 2.25a_s$, is examined in Fig. 5(c). Large values of δ_{IR} strongly increase the SB amplitudes, as a large volume of the substrate is exposed to the IR light. In Fig. 5(d) we quantify the energy-profile dependence on the initial-state probability-density-decay parameter E_{TB}. We achieve the best overall agreement with the measured HH and SB amplitudes in [11] by setting E_{TB} equal to the central energy of the measured Cu(111) *d*-band profile [26].

Lucchini *et al.* [11] obtained Cu(111) RABBITT phases ϕ^{RAB}_{2n} by (i) eliminating the unkown HH phases using interferograms measured on gaseous Ne as a reference and (ii) substituting the Ne atomic phases with calculated phases of Ref. [8]. In our calculations, we set all XUV HH phases to zero, resulting in RABBITT phases ϕ^{RAB}_{2n} comparable to the experimental values. We obtain ϕ^{RAB}_{2n} by fitting with parameters $a_{1,\ldots,5}$ our calculated photoelectron yields, integrated over 0.3 eV intervals around the given SB_{2n} energy, to the expression [11]

$$\left[a_1 \cos\left(2\omega_{IR}\left(\tau - a_3\right) + \phi^{RAB}_{2n}\right) + a_2\right] e^{-\left[\frac{(\tau - a_3)}{a_4}\right]^2} + a_5.$$

For 75° incidence Fig. 6 reveals that our quantum-mechanical calculations and the semiclassical Monte-Carlo (MC) simulations of [11] have an overall shift of ≈ -0.5 rad (≈-100 attoseconds) with respect to the experimental phases. Two fundamentally different theories pointing to the same offset relative to the measured Cu(111) phases may indicate either (i) an anisotropic behaviour of the dielectric constant not accounted for by our isotropic $\varepsilon(\omega_{IR})$ model, or (ii) the limitation of our translationally invariant initial-state model.

In summary, comparing our calculated RABBITT spectra and phases for Cu(111) with experimental data [11], we find that our localized-orbital initial-state expansion and inclusion of the potential-step at the surface in the final state provide spectra in good agreement with the measurements. In addition, our model explains the measured SB temporal-width broadening and HH narrowing as due to four-IR-photon-interference pathways. We find the Cu(111) RABBITT energy profile to be fairly robust with regard to variations of the simulation parameters λ, U_0, δ_{IR}, and E_{TB}. The potential well depth U_0 affecting the final state modifies the yields the most. This seemingly simple adjustment to the final

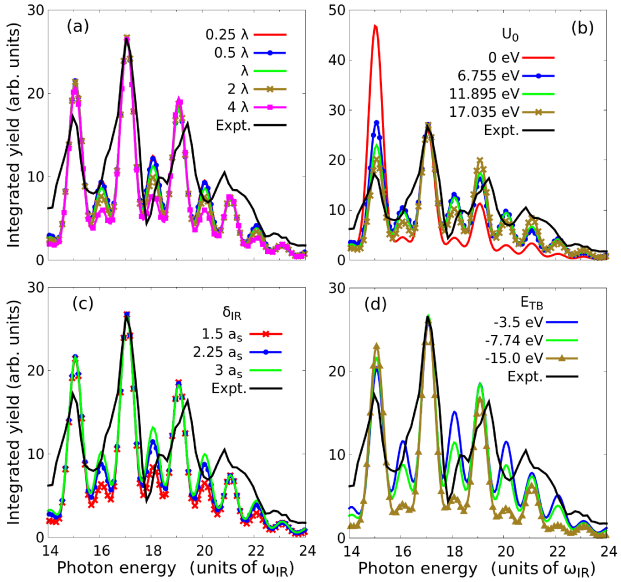

Figure 5: (Color online) Parameter dependence of delay-integrated yields as functions of the photon energy for single-parameter variations from the best experiment-matching set: $\lambda(\varepsilon_f)$ from [23], $U_0 = 17.035$ eV, $\delta_{IR} = 2.25a_s$, and $E_{TB} = E_b = -7.74$ eV. Sensitivity to changes in (a) $\lambda(\varepsilon_f)$, (b) U_0, (c) δ_{IR}, and (d) E_{TB}. Experimental yield adapted from Ref. [11].

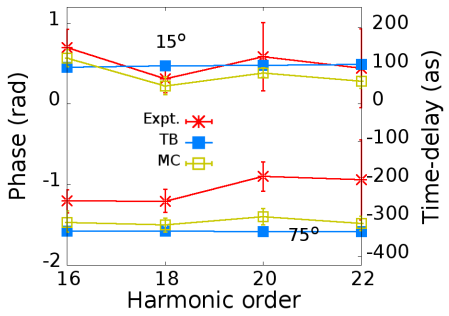

Figure 6: (Color online) RABBITT phases ϕ_{2n}^{RAB} extracted from our calculated spectra in Fig. 2 in comparison with the experimental and simulated (MC) results from Ref. [11].

state noticeably improves the agreement with the experiment and emphasizes the sensitivity of the RABBITT spectra on the electron-emission dynamics near solid surfaces. An IR-skin-depth increase (decrease) visibly increases (decreases) the SB yields relative to HH yields. Mean-free-path effects on the energy profile are moderate. The most favorable comparison with the experimental energy profile is achieved when the orbital asymptotic decay is characterized by the $3d$-band binding energy. Our RABBITT phases are strongly affected by the inclusion of the Fresnel-reflected IR pulse and in reasonable agreement with the classical simulations in [11].

We thank M. Lucchini and U. Keller for providing experimental data and L. Argenti for useful comments. This work was supported by NSF grant PHY-1464417 and the Division of Chemical Sciences, Office of the Basic Energy Sciences, Office of Energy Research, US DoE.

[1] C.-G. Wahlström, J. Larsson, A. Persson, T. Starczewski, S. Svanberg, P. Salières, P. Balcou, and A. L'Huillier, Phys. Rev. A **48**, 4709 (1993).
[2] K. J. Schafer and K. C. Kulander, Phys. Rev. Lett. **78**, 638 (1997).
[3] P. M. Paul, E. S. Toma, P. Breger, G. Mullot, F. Augé, P. Balcou, H. G. Muller, and P. Agostini, Science **292**, 1689 (2001).
[4] G. Sansone, E. Benedetti, F. Calegari, C. Vozzi, L. Avaldi, R. Flammini, L. Poletto, P. Villoresi, C. Altucci, R. Velotta, S. Stagira, S. De Silvestri, and M. Nisoli, Science **314**, 443 (2006).
[5] E. Goulielmakis, M. Schultze, M. Hofstetter, V. S. Yakovlev, J. Gagnon, M. Uiberacker, A. L. Aquila, E. M. Gullikson, D. T. Attwood, R. Kienberger, F. Krausz, and U. Kleineberg, Science **320**, 1614 (2008).
[6] B. H. Bransden and C. J. Joachain, *Physics of atoms and molecules* (Englewood Cliffs, NJ, Prentice–Hall, 2003).
[7] U. Thumm, Q. Liao, E. M. Bothschafter, F. Süßmann, M. F. Kling, and R. Kienberger, in *The Oxford Handbook of Innovation*, edited by D. Andrew (Wiley, New York, 2015), chap. 13.
[8] J. Mauritsson, M. B. Gaarde, and K. J. Schafer, Phys. Rev. A **72**, 013401 (2005).
[9] K. Klünder, J. M. Dahlström, M. Gisselbrecht, T. Fordell, M. Swoboda, D. Guénot, P. Johnsson, J. Caillat, J. Mauritsson, A. Maquet, R. Taïeb and A. L'Huillier, Phys. Rev. Lett. **106**, 143002 (2011).
[10] R. Locher, L. Castiglioni, M. Lucchini, M. Greif, L. Gallmann, J. Osterwalder, M. Hengsberger, and U. Keller, Optica **2**, 405 (2015).
[11] M. Lucchini, L. Castiglioni, L. Kasmi, P. Kliuiev, A. Ludwig, M. Greif, J. Osterwalder, M. Hengsberger, L. Gallmann, and U. Keller, Phys. Rev. Lett. **115**, 137401 (2015).
[12] Z. Tao, C. Chen, T. Szilvási, M. Keller, M. Mavrikakis, H. Kapteyn, and M. Murnane, Science **353**, 62 (2016).
[13] C. Chen, Z. Tao, A. Carr, P. Matyba, T. Szilvási, S. Emmerich, M. Piecuch, M. Keller, D. Zusin, S. Eich, M. Rollinger, W. You, S. Mathias, U. Thumm, M. Mavrikakis, *et al.*, Proc. Natl. Acad. Sci. USA **114**, E5300, (2017).
[14] M. Lucchini, A. Ludwig, L. Kasmi, L. Gallmann, and U. Keller, Opt. Express **23**, 8867 (2015).
[15] M. J. Ambrosio and U. Thumm, Phys. Rev. A **94**, 063424 (2016).
[16] C.-H. Zhang and U. Thumm, Phys. Rev. A **80**, 032902 (2009).
[17] Q. Liao and U. Thumm, Phys. Rev. A **89**, 033849 (2014).
[18] N. E. Christensen and B. O. Seraphin, Phys. Rev. B **4**, 3321 (1971).
[19] M. S. Gravielle, M. Alducin, J. I. Juaristi, and V. M. Silkin, Phys. Rev. A **76**, 044901 (2007).
[20] M. J. Ambrosio, J. A. Del Punta, K. V. Rodriguez, G. Gasaneo, and L. U. Ancarani, J. Phys. A **45**, 015201 (2012).
[21] A. L. Frapiccini, G. Gasaneo, F. Colavecchia, and D. Mitnik, J. Electron Spectrosc. **161**, 199 (2007).
[22] E. Chulkov, V. Silkin, and P. Echenique, Surf. Sci. **437**, 330 (1999).
[23] S. Tanuma, C. J. Powell, and D. R. Penn, Surf. Interface Anal. **43**, 689 (2011).
[24] W. Greiner, *Classical Electromagnetism* (Springer, New York, 1996).
[25] A. D. Rakić, A. B. Djurišić, J. M. Elazar, and M. L. Majewski, Appl. Opt. **37**, 5271 (1998).
[26] F. Roth, C. Lupulescu, E. Darlatt, A. Gottwald, and W. Eberhardt, J. Electron Spectrosc. **208**, 2 (2016).